Advanced Powder Technology (2013). 24(5), 852-857.
DOI: http://dx.doi.org/10.1016/j.apt.2013.03.011

Aerosol route as a feasible bottom-up chemical approach for up-converting phosphor particles processing

I. Dugandžić [a], V. Lojpur [a], L. Mančić [a], M.D. Dramićanin [b], M.E. Rabanal [c], T. Hashishin [d], Z. Tan [d], S. Ohara [d], O. Miloševic´ [a,*]

[a] Institute of Technical Sciences of SASA, K. Mihailova 35/IV, 11000 Belgrade, Serbia
[b] Vinca Institute of Nuclear Sciences, University of Belgrade, 11001 Belgrade, Serbia
[c] University Carlos III, Avd. Universidad 30, 28911 Leganes, Madrid, Spain
[d] Joining and Welding Research Institute, Osaka University, 11-1 Mihogaoka, Ibaraki, Osaka 567-0047, Japan
* Corresponding author. Tel.: +381 11 2636994; fax: +381 11 2185263. E-mail address: olivera.milosevic@itn.sanu.ac.rs (O. Miloševic´).

Abstract: The opportunities of the hot wall aerosol synthesis, i.e. conventional spray pyrolysis (CSP) method are demonstrated for the generation of highly spherical three-dimensional (3D) nanostructured phosphor particles with uniformly distributed components, phases and nano-clustered inner structure. With the presumption that certain particle morphology is formed during the evaporation/drying stage, the aerosol transport properties and powder generation are correlated with the particles structural and morpholog-ical features. With the help of various analyzing techniques like Field Emission Scanning Electron Micros-copy (FE-SEM), Transmission Electron Microscopy (TEM) coupled with energy dispersive X-ray Analysis and STEM mode (TEM/EDS), X-ray Powder Diffraction (XRPD) and fluorescence measurements the feasi-ble processing of up-conversion rare-earth Y_2O_3:Er, Yb phosphors powders are discussed.

Keywords: Aerosol, Yttrium oxide, Morphology, Phosphors, Up-conversion

1. Introduction

Rare-earth based up-converting phosphor (UCP) nanocrystalline particles represent the new, sophisticated generation in materials science and engineering with the potential use in modern display and labeling technologies, sensors, optical data storage, telecommunications, etc. [1–5]. They exhibit the unique property of emitting visible light following photoexcitation in near infrared region. The most efficient up-converting host materials belong to the group of the yttrium based- inorganic compounds like fluorides, oxides and oxysulfides codoped with the trivalent rare earths (Yb^{3+}, Er^{3+}, Tm^{3+}, Pr^{3+}, Ho^{3+}, etc.). Among other yttrium compounds, yttrium oxide represents an efficient UCP phosphor host material for the substitution of rare earth ions because of its low phonon energy, <600 cm^{-1}, broad optical transparency range 0.2–8 μm, high refractive index, >1.9 and large energy band-gap, 5.8 eV [6]. Yttrium oxide posses a cubic crystal structure with a space group, S.G. *Ia3*-(T_h^7) in which there are two crystallographically different rare-earth sites, C2 (75%) and S6 (25%); by that, a unit cell is composed of four atom positions, three having a point symmetry C2 and one position with a point symmetry S6 [7].

High luminescence efficiency is basically associated with high radiative transition rates which can be achieved with optimum doping concentration, uniform distribution of the luminescent centers in the host matrix and the overall particle structure and morphology control, which altogether signify the importance of innovative and controllable UCP phosphor processing route in the current research efforts [7–9]. Moreover, of particular impor-tance is the controlled synthesis of the host lattice having targeting crystal structure which determines the distance between the dop-ant ions, their relative spatial position, their coordination numbers, and the type of anions surrounding the dopant. In addition, the low symmetry and low phonon energies of the host lattice are essential for reducing the multiphonon relaxation and increasing the life-time of the intermediate states involved in upconversion [10]. Most of research are concerned with halide host matrix processing and particularly with the hexagonal sodium yttrium fluoride which has been regarded as one of the most efficient up conversion host matrix having the phonon energies below 500 cm^{-1} [11–13]. O f the medium phonon energies host matrices, cubic yttria posses high chemical and thermal stability and is one of the most efficient non-halide host material [11].

Among the diversity of the "bottom-up" chemical approaches for nanomaterials processing, synthesis through dispersion phase (aerosol) enables generation of ultrafine, either single or complex powders with controlled stoichiometry, chemical and phase con-

Nomenclature

c_i	initial precursor solution concentration (mol dm$^{-3)}$
d_d	droplet diameter (m)
d_p	particle diameter (m)
D	tube diameter (m)
L	tube length (m)
F_a	flow rate of gas phase (carrier gas, air) (m^3 s^{-1})
h_t	heat transfer coefficient (J s^{-1} m^{-2} K^{-1})
k_w	thermal conductivity (W m^{-1} K^{-1})
M	molecular weight (g mol^{-1})
T	temperature (K)
t	time (s)
u_a	mean velocity of gas phase (carrier gas, air) (m s^{-1})

Greek letters

γ	surface tension of precursor (N m^{-1})
μ	shear viscosity of gas/liquid phase (m Pas)
ρ	density of gas/liquid phase (kg m^{-3})
τ	residence time of droplets/particles (s)
φ	volume fraction of solute [1]
φ^*	critical volume fraction of solute [1]

Dimensionless number

Bi	Biote number [1]
Nu	Nusselt number [1]
Re	flow Reynolds number [1]
Re_t	particle Reynolds number [1]

Subscripts

a	air
d	droplets
i	initial precursor solution
p	particles
w	water

Equations

d_d	$0.34 \cdot \left(\frac{8 \cdot \pi \cdot \gamma_i}{\rho_i \cdot f^2}\right)^{1/3}$
d_p	$d_d \cdot \left(\frac{c_i M_{Y_2O_3}}{\rho_{Y_2O_3}}\right)^{1/3}$
φ	$\varphi = \frac{c_i \cdot M_{Y_2O_3}}{1000 \cdot \rho_i}$

tent provided by high heating and cooling rates, short residence time and high surface reaction [14]. This may favors to the formation of either amorphous, nanocrystalline or metastable phases that might have a huge impact in the processing of advanced functional materials having novel and unique structures and properties. During the process, aerosol droplets undergo evaporation, drying and solute precipitation in a single-step, enabling spherical, either hollow or dense, agglomerate-free, submicronic "secondary" particles to be obtained exhibiting the composite inner nanostructure and representing an assembly of primary nanoparticles. The size and size distribution of secondary particles are mainly influenced by the properties of precursor solutions and aerosol generation, while the size of primary particles depends on the time–temperature history of particle formation and materials properties [7]. There is a diversity of aerosol routes, depending mainly on the manner of aerosol formation and how the aerosol decomposition energy is transferred to the precursor system, reflecting on the most important particle formation parameters: residence time and temperature distribution [7]. Among them, flame synthesis represents a straightforward large-scale aerosol route for producing spherical nanoparticles in different oxide and non-oxide systems, enabling higher temperatures and shorter residence time to be obtained. It has been reported a successful processing of nanocrystalline up conversion phosphor particles in Yb (Tm, Er) doped-sodium yttrium fluoride and Sm-doped Gd_2O_3 by this route [13,15]. For the case of hot-wall flow reactor, a well-controlled temperature profile over long residence times can be achieved, however the direct processing of nanoscaled particles is limited and associated either with the precursor solution dilution or urea/salt assisted solution modification [7], which in turn influence on the powder production rates.

In our previous work, hot wall aerosol route has been recognized as successfull to obtain submicronic Eu^{3+}-doped nanocrystalline down-conversion Y_2O_3, $(Y_{1-x}Gd_x)_2O_3$ and Gd_2O_3 phosphor particles with advanced structural, morphological and luminescent properties [8,9,16]. It has been demonstrated that the key particle formation parameters are the physico-chemical properties of precursor solution, the manner of aerosol generation and the process parameters like temperature, residence time, and atmosphere determining the mechanisms of aerosol formation, solute precipitation, nucleation, growth and primary nanoparticles aggregation into a spherical assemblage [7]. Recently we have presented the aerosol processing of temperature sensitive Y_2O_3 based nanocrystalline UCP particles, doped with Yb^{3+} and co-doped with either Tm^{3+} or Ho^{3+} [17]. Considering the diversity applications of nanocrystalline up-converting particles and especially their potential advantages over micro-scaled conventional materials, in this work we have prepared yttrium oxide co-doped with erbium and ytterbium by applying the same aerosol based conventional spray pyrolysis (CSP) method. Aiming to investigate the morphology aspect of UCP nanocrystalline particles, we have studied droplet-to-particle formation mechanisms in dispersed system and have discussed them in the framework of the obtained structural, morphological and spectroscopic properties.

2. Experimental

In order to synthesize $Y_{1.94}Yb_{0.05}Er_{0.01}O_3$ UCP particles, the precursor aqueous solutions (c_i = 0.1 mol/dm^3) are prepared by dissolving the corresponding amounts of $Y(NO_3) \times 6H_2O$, $Yb(NO_3) \times 5H_2O$ and $Er(NO_3) \times 5H_2O$ having Yb/Er concentration ratio 5. All the chemicals are of the highest purity available (Aldrich, 99%); distilled deionized water is used with a resistivity of 18.2 MΩ cm^{-1} (Milipore, UK). The obtained precursor solution is further ultrasonically atomized and such obtained aerosol is decomposed in the air stream in a high-temperature tubular flow reactor (tube geometry: D = 0.04 m; L = 1.9 m) equipped with the three temperature zones (T_1 = 473, T_2 = 1173, T_3 = 1173 K). The as-prepared powders are subjected to the additional thermal treatment in air at 1373 K for 12, 24 and 48 h (samples 5-2, 5-3 and 5-4), while 5-1 denotes as-prepared powder sample. The details regarding the processing route are given elsewhere [7] and schematic of the conventional spray pyrolysis experimental setup is presented at Fig. 1.

Physico-chemical properties of the precursor solutions are estimated at room temperature. Particle size distribution is analysed by laser particle sizer (Mastersizer 2000, Malvern Instruments). The morphological analysis and chemical purity are investigated by Field Emission Scanning Electron Microscopy, HITACHI SU-70 (FESEM) and Transmission Electron Microscopy, JEOL, JEM-2100F, 200 kV (TEM) coupled with energy dispersive X-ray Analysis and STEM mode. Structural evaluation is done by X-ray powder diffrac-

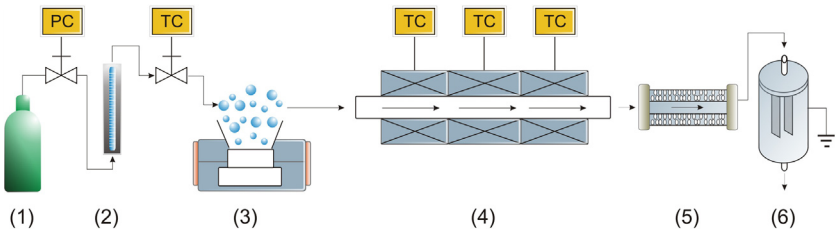

Fig. 1. Schematic representation of the laboratory setup of CSP with (1) carrier gas, (2) flow meter, (3) ultrasonic atomizer, 1.3 MHz, RBI (4) hot-wall reactor (5) diffusion dryer, TSI and (6) electrostatic precipitator.

tion (XRPD) analysis on Rigaku Ultima IV diffractometer operating with Cu Kα radiation at 40 mA and 40 kV. The measurements are performed in the 2θ range from 10° to 100° with a step scan of 0.02 and counting time of 10 s per each step. The Rietveld structural refinement is done in Topas Academic 4.1 [18] for the determination of microstructural parameters using the Fundamental Parameter Approach where FWHM based LVol (volume weighted mean column height) calculation is used for the determination of the intermediate crystallite size broadening modeled by a Voigt function. The photoluminescence spectra and decay time measurements are performed on spectroflurometer system having optical parametric oscillator excitation source, (Impulse laser −2 mJ per pulse, pulse duration 5.2 ns, repetition rate 10 Hz, EKSPLA NT 342, emission range 210–2300 nm), Cryostat (Advance Research Systems DE202-AE) equipped with Lakeshore model 331 controller, spectrograph FHR 1000 (Horiba Jobin–Yvon, 300 groove/mm grating) and ICCD detector (Horiba Jobin–Yvon 3771). The single exponential function is used for the decay time fitting.

3. Results and discussion

With the presumption that certain particle morphology is formed during the evaporation/drying stage of CSP [19,20], all calculations related to the aerosol transport regimes are estimated at 373.15 K. Moreover, considering a one-droplet- to one-particle conversion mechanism [21], the mean gas velocity and residence time were calculated from the gas flow rate and the geometry of hot-wall reactor aiming to analyze the conditions for particle generation in dispersed system. Based on that, the Reynolds number of the air flowing around single droplet/particle, defined as:

$$\mathrm{Re}_t = \frac{\rho_a \cdot d_d \cdot u_\mathrm{a}}{\mu_a} \tag{1}$$

imply laminar gas motion; d_d is the droplet diameter, 3.217 μm, estimated in accordance to the Lang equitation and the solution properties, [22–24], while the values and definition of other parameters are given in Table 1 and/or in Notations. It is assumed droplet-to-droplet interaction are negligible because of the small droplet volume fraction in continuous phase [25].

The Reynold's number, which defines the regime of the aerosol transport within the system:

$$\mathrm{Re} = \frac{\rho_a \cdot D \cdot u_a}{\mu_a} \tag{2}$$

is calculated to be Re ∼ 36.70 <2300, implying the aerosol transportation is done within the carrying gas into a laminar flux motion.

The temperature distribution along the radius of a droplet could be ignored for Biot number, Bi < 1, in accordance to the following equitation:

$$\mathrm{Bi} = \frac{h_t \cdot d_d}{6 \cdot k_w} \tag{3}$$

in which k_w (W m^{-1} K^{-1}) is the droplet thermal conductivity, 0.683, taken for water at 373.15 K With assumption the droplet velocity is the same as that of the carrier gas, the heat transfer coefficient, h_t, is estimated based on Nusselt and Prandtl dimensionless numbers (Table 1) by combining the following equations:

$$\mathrm{Nu} = 2 + 0.6 \cdot \mathrm{Re}_t^{1/2} \cdot P_r^{1/3} \tag{4}$$

and

$$\mathrm{Nu} = \frac{h_t \cdot d_d}{k_w} \tag{5}$$

Because the resistance to heat flow within the droplet is small relative to the resistance presented by the convection processes at the surface, the temperature inside the droplet is uniform and assumed to be the same as the droplet surface, implying volume precipitation of solute inside the droplet. This implicates solid particle formation if the precolation criterion is fulfilled, enabling formation a continuous three-dimensional network of solute filling.

Table 1
The solution/gas properties and conditions for aerosol transport and particle generation.

The conditions for particle generation in a dispersed system				
Carrier Gas (air) flow rate, $F_a \times 10^5$ (m^3 s^{-1})		Mean velocity of carrier gas, u_a (m s^{-1})		Residence time, τ (s)
2.667		0.02123		89.5
Physico-chemical and transport properties of air at T = 373.15 K				
Density, ρ_a (kg m^{-3})	Shear viscosity, $\mu_a \times 10^6$ (Pas)	Pr	Re	Transport regime
0.946	2.19	0.688	36.70	<2.3 × 10^3 laminar
Physico-chemical properties of the precursor solution at 298 K				
Concentration, c_i (mol dm^{-3})	Surface tension, $\gamma_i \times 10^3$ (N m^{-1})	Viscosity, μ_i (m Pas)		Density, $\rho_i \times 10^{-3}$ (kg m^{-3})
0.1	65.8	1.058		1.02217
Values of dimensionless numbers and heat transfer coefficient at T = 373.15 K				
$\mathrm{Re}_t \times 10^3$ [1]	Nu [1]	$h_t \times 10^{-5}$ (W m^{-1} K^{-1})	Bi [1]	φ
3.039	2.029	4.183	0.338	0.00459 < 0.16

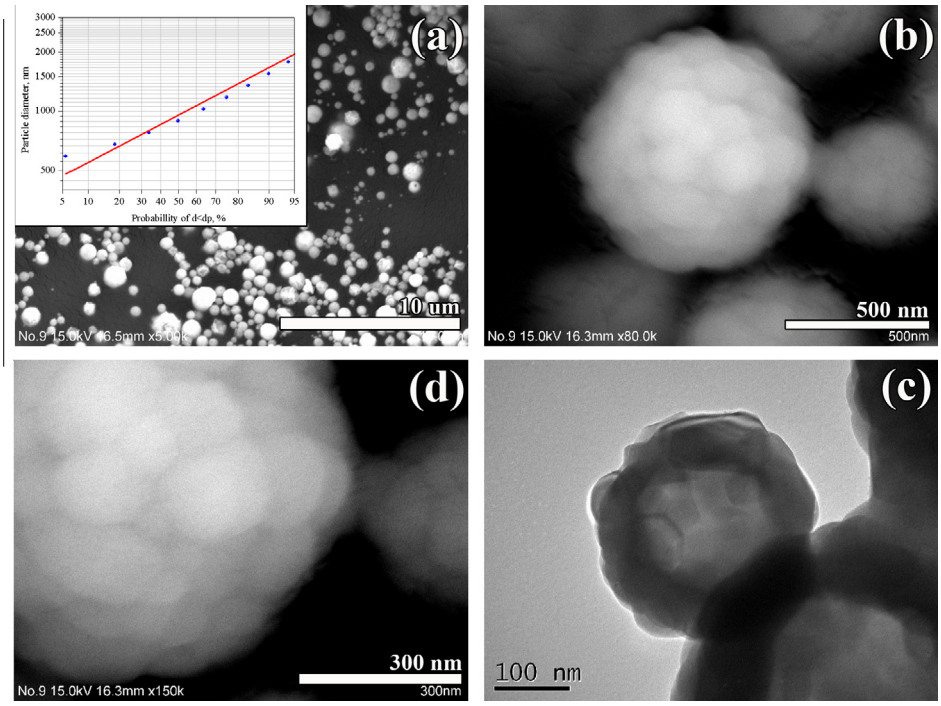

Fig. 2. FESEM micrographs of as-prepared (a) and powders heat treated at 1373 K for 24 h (b and c); low magnification TEM image of the powder 1373 K for 24 h (d); the corresponding log-probability plot is given in inset.

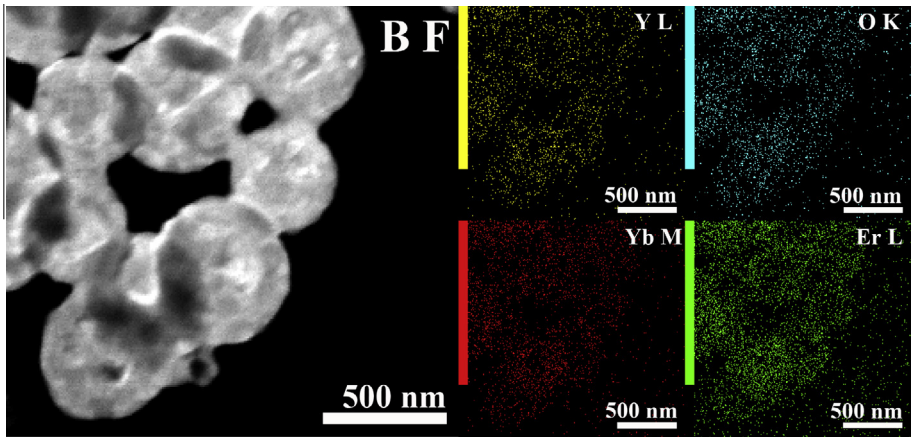

Fig. 3. STEM image and EDS mapping of $Y_{1.94}Yb_{0.05}Er_{0.01}O_3$ UCP particles (SP 5-3).

However, for the conditions in this experimental work, the percolation criterion, φ is less than the critical volume fraction $\varphi^* = 0.16$ [20], implying the possibility for excessive porosity formation.

FE-SEM micrographs are presented at Fig. 2 for as-prepared and thermally treated powder samples. The presence of polydispersed spherical particles in submicronic range is evident. Either the sponge-like or desert-rose-like particle morphology prevailed for the as-prepared powders, while the prolonged heating leads to the better differentiation of primary particles as a result of their thermally induced growth, collision and aggregation. The as-prepared particle distribution is log-normal, as evident from Fig. 2a inset, with the $D_{50} = 985$ nm. The typical particle morphology after thermal treatment at 1373 K/24 h is presented at Fig. 2b and c, showing the blueberry-like structure of secondary particles representing an assembly of nanosized (<50 nm) primary particles. The primary particles are predominantly spherical in shape, colliding to the aggregates. Moreover, the increase of the annealing temperature and time additionally leads to the interparticle sintering that is more prominent at higher temperatures. Low magnification

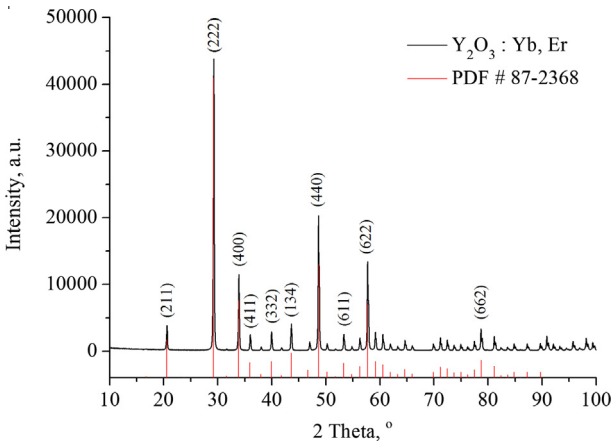

Fig. 4. XRD pattern of $Y_{1.94}Yb_{0.05}Er_{0.01}O_3$ UCP particles annealed at 1373 K/24 h (SP 5-3).

Table 2
Rietveld refinement of $Y_{1.94}Yb_{0.05}Er_{0.01}O_3$ UCP particles (SP 5-3).

Lattice parameter (Å)	Crystallite size (nm)	[a]Y_1:O bond length (Å)	[a]Y_2:O bond length (Å)	Y_1	O^{2-}	Occ Y_1 (Y3+)	Occ $Y_2(Y^{3+})$	R_{Bragg}
10.59915 (6)	69 (1)	2.216 (4) 2.267 (4) 2.340 (4)	2.283 (4)	x – 0.0321(1)	x 0.3953 (4) y 0.1554 (3) z 0.3778 (3)	0.9693	0.9721	2.69

[a] Y_1 corresponds to C_2 site; Y_2 corresponds to S_6 site in cubic crystal unit cell, S.G. *Ia-3*.

TEM implies the higher particle density at the surface implicating the particles predominantly aroused through the mechanism of surface precipitation [7]. Based on the elemental analysis (Fig. 3) it is evident a very homogeneous distribution of the constitutive elements: Y (Lα, 1.9226 keV), O (Kα 0.5249), Er (Lα 6.9488 keV), Yb (Mα 1.5215 keV). That represents one of the basic advantage of CSP showing no compositional segregation at the selected particle agglomerate presented in STEM image (upper left). Moreover, a uniform distribution of the Yb^{3+} and Er^{3+} ions into a host yttria matrix implicates high luminescence efficiency to be obtained.

XRPD analysis confirms the presence of a single cubic bixbyte crystal structure (S.G. *Ia-3*, PDF 87-2368) in all synthesized and thermally treated samples. The much narrower peak reflections are observed in thermally treated powders implying the increase of crystallinity with annealing temperature and time. Detailed microstructural analysis performed for SP-5-3 powder sample through Rietveld refinement (Fig. 4 and Table 2) revealed the crystal cell parameters did not change significantly after dopants incorporation in comparison to the Y_2O_3 phase (PDF 89-5591, a = 10.6 Å) due to the small differences in their ionic radii (Y^{3+} 0.104 Å, Yb^{3+} 0.100 Å, Er^{3+} 0.103 Å). After incorporation into the Y_2O_3 matrix, the Yb^{3+} and Er^{3+} ions could be randomly distributed into the two nonequivalent crystallographic sites: non-centrosymmetric C_2 at the 24d site and centrosymmetric S_6 (C_{3i}) at the 8a site [9]. With regards to that the Y^{3+} cation site occupancy refinements of both positions were performed, since the preferential occupation might influence on luminescence efficiency. The obtained results imply that substitution of Y^{3+} is more pronounced in the C_2 position than in S_6 position, as indicated by the lower values for C_2 site occupation with Y^{3+}, Table 2. It is estimated the crystallite size of about 70 nm for the SP 5-3 sample thermally treated at 1373 K/24 h, confirming the powder nanocrystalline structure.

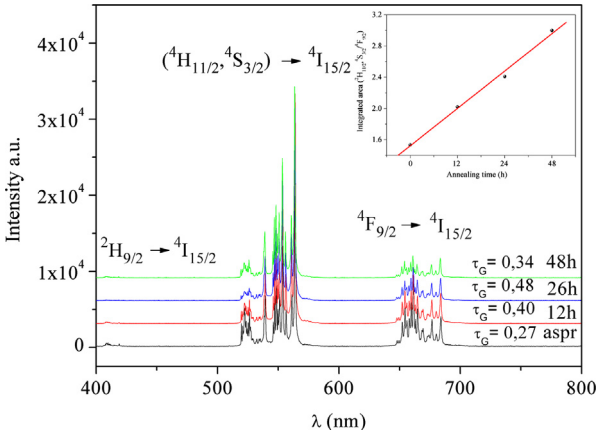

Fig. 5. Up-conversion emission spectra of nanocrystalline $Y_{1.94}Yb_{0.05}Er_{0.01}O_3$ powders excited at 978 nm as a function of annealing time at 1373 K, with the corresponding decay times, τ_G (ms). The annealing time dependence of green to red emission integrated area ratio is presented in inset. (For interpretation of the references to color in this figure legend, the reader is referred to the web version of this article.)

The up-conversion luminescence spectra upon excitation at 978 nm are presented at Fig. 5 as a function of annealing time at 1373 K. The green luminescence emission, assigned to the Er^{3+} ($^2H_{11/2}$, $^4S_{3/2}$) → $^4I_{15/2}$ electronic transitions is evident, peaking at 563 nm. The red emission at 660 nm is less intensive, and corresponds to the Er^{3+} $^4F_{9/2}$ → $^4I_{15/2}$ electronic transitions, while weak blue emission, assigned to the Er^{3+} $^2H_{9/2}$ → $^4I_{15/2}$ electronic transitions is almost negligible. The annealing time dependence of green to red emission integrated area ratio, presented at Fig. 5 in inset, increases linearly. It is assumed that due to the smallest energy levels band gap, the ($^2H_{11/2}$, $^4S_{3/2}$) → $^4I_{15/2}$ electronic transition is more affected by the phonons adsorbed at the surface comparing to the $^4F_{9/2}$ → $^4I_{15/2}$ ones [4]. By that, the thermally and kinetically provoked crystallite/particle growth and the surface defects diminishing manifest in increase of green to red emission ratio with annealing time.

The corresponding decay times at 300 K for the most prominent green emission, τ_G (ms), are presented at the Fig. 5, as well. For the rare earth ions is typical longer excited-state lifetimes, 10^{-6}–10^{-3} s compared to 10^{-9}–10^{-6} s for conventional ions [26]. The obtained decay time values associated with long emission implied very good up-conversion efficiency of powders and are improved in comparison to the reported values for nanocrystalline materials [11,27]. The higher value of 0.48 ms is obtained after 1373 K/24 h annealing. With no doubt, the observed relationship of the emission spectra and the decay times with annealing conditions are closely associated with the particle structure and morphology i.e. increasing the crystallite size associated with lowering of the defects and better accommodation of dopants into the lattice sites. In the same time, the counter current process of particle aggregation occurs, as evident by the neck formation and thickened with annealing, which causes the decrease of decay time after 48 h annealing. These altogether implies the optimum luminescence efficiency is a compromise of the time/temperature evolution of particle structure and morphology. The particles structural and morphological features (submicronic in size, spherical, nanostructured, having uniform distribution of the luminescent center) imply their application in different up converting phosphor technologies like security labeling, forensic, light emitting devices, temperature sensors, etc. [17]. Moreover, the particles composite inner structure, representing an assembly of nanosized primary particles, opens the possibility for particle surface modification and functionalization emphasizing the possibility in bioimaging and energy transfer applications [26].

4. Conclusions

Aerosol route as a bottom-up chemical approach for UCP phosphor particles processing is presented together with the corresponding process parameters that influence on the particle structure, morphology and composition. With the presumption that certain particle morphology is formed during the evaporation/drying stage of CSP, droplet to particle conversion and transport properties in dispersed system were followed using Re, Nu, Pr and Bi dimensionless numbers. The structural, morphological and functional properties, analyzed in accordance to XRPD, FESEM,

STEM, TEM and spectroscopic measurements proved the feasibility of CSP for nanocrystalline phosphor particle processing.

Acknowledgements

The financial support for this work is provided by the Ministry of Education, Science and Technological Development of the Republic of Serbia Project No. 172035 and JSPS fellowship, 2011/2012 (O.M.).

References

[1] G. De, W. Qin, J. Zhang, J. Zhang, Y. Wang, C. Cao, Y. Cui, Upconversion luminescent properties of Y_2O_3:Yb^{3+}, Er^{3+} nanostructures, J. Lumin. 119 (2006) 258–263.

[2] X. Hou, S. Zhou, W. Li, Y. Li, H. Lin, H. Teng, T. Jia, Investigation of Up-conversion luminescence in Er^{3+}/Yb^{3+} – codoped yttria transparent ceramics, J. Am. Ceram. Soc. 93 (2010) 2779–2782.

[3] A.O.G. Dikovska, P.A. Atanasov, M. Jimenez de Castro, A. Perea, J. Gonzalo, C.N. Afonso, J. Garcia Lopez, Optically active Er^{3+}–Yb^{3+} codoped Y_2O_3 films produced by pulsed laser deposition, Thin Solid Films 500 (2006) 336–340.

[4] A.M. Pires, S. Heer, H.U. Gudel, O.A. Serra, Er, Yb doped yttrium based nanosized phosphors: particle size, ''host lattice'' and doping ion concentration effects on upconversion efficiency, J. Fluoresc. 16 (2006) 461–468.

[5] D. Vennerberg, Z. Lin, Upconversion nanocrystals: synthesis, properties, assembly and applications, Sci. Adv. Mater. 3 (2011) 26–40.

[6] A.J. Martinez, L.A. Morales, Diaz-Torres, P. Salas, E. De la Rosa, J. Oliva, H. Desirena, Green and red upconverted emission of hydrothermal synthesized Y_2O_3:Er^{3+}–Yb^{3+} nanophosphors using different solvent ratio conditions, Mater. Sci. Eng. B 174 (2010) 164–168.

[7] O. Milosevic, L. Mancic, M.E. Rabanal, L.S. Gomez, K. Marinkovic, KONA Powder Part. J. 27 (2009) 84–106.

[8] O. Milosevic, L. Mancic, M.E. Rabanal, B. Yang, P.D. Townsend, Structural and luminescence properties of Gd_2O_3:Eu^{3+} and $Y_3Al_5O_{12}$:Ce^{3+} phosphor particles synthesized *via* aerosol, J. Electrochem. Soc. 152 (9) (2005) G707–G713.

[9] K. Marinkovic, L. Mancic, L.S. Gomez, M.E. Rabanal, M. Dramicanin, O. Milosevic, Photoluminescent properties of nanostructured Y_2O_3:Eu^{3+} powders obtained through aerosol synthesis, Opt. Mater. 32 (2010). 1606–161.

[10] T. Zhang, L. Yu, J. Wang, J. Wu, Microstructure and up-conversion luminescence of Yb^{3+} and Ho^{3+} co-doped BST tick films, J. Mater. Sci. 45 (24) (2010) 6819–6823.

[11] X.X. Luo, W.H. Cao, Blue green red upconversion luminescence and optical characteristics of rare earth doped rare earth oxide and oxysulfide, Sci. Chin. Ser. B: Chem. 50 (4) (2007) 505–513.

[12] Q. Wang, M.C. Tan, R. Zhuo, G.A. Kumar, R.E. Riman, A solvothermal route to size- and phase-controlled highly luminescent NaYF4:Yb, Er up-conversion nanocrystals, J. Nanosci. Nanotechnol. 10 (2010) 1685–1692.

[13] A. Stepuk, W.K. Kramer, J.W. Stark, Flame synthesis of complex fluoride- based nanoparticles as upconversion phosphors, KONA Powder Part. J. 30 (2013) 267–275.

[14] B.D. Nandiyanto, K. Okuyama, Progress in developing spray-drying methods for the production of controlled morphology particles: from the nanometer to submicrometer size ranges, Adv. Powder Technol. 22 (2011) 1–19.

[15] D. Dosev, I.M. Kennedy, M. Godlewski, I. Gryczynski, K. Tomsia, E.M. Goldysa, Fluorescence upconversion in Sm-doped Gd_2O_3, Appl. Phys. Lett. 88 (2006) 011906-1–011906-3.

[16] L. Mancic L, B.A. Marinkovic, K. Marinkovic, M. Dramicanin, O. Milosevic, Soft chemistry routes for synthesis of rare earth oxide nanoparticles with well defined morphological and structural characteristics, J. Nanopart. Res. 13 (11) (2011) 5887–5897, http://dx.doi.org/10.1007/s11051-010-0215-9.

[17] V. Lojpur, M. Nikolic, L. Mancic, O. Milosevic, M.D. Dramicanin, Y_2O_3:Yb, Tm and Y_2O_3:Yb, Ho powders for low-temperature thermopmetry based on up-conversion luminescence, Ceram. Int. 39 (2) (2012) 1129–1134.

[18] A.A. Coelho, Topas – Academic, 2006.

[19] O. Milosevic, V. Gagic, J. Vodnik, A. Mitrovic, L.J. Karanovic, B. Stojanovic, L.J. Zivkovic, Synthesis and deposition of ZnO based particles by aerosol spray pyrolysis, Thin Solid Films 296 (1997) 44–48.

[20] G.L. Messing, S.-C. Zhang, G.V. Jayanthi, Ceramic powder synthesis by spray pyrolysis, J. Am. Ceram. Soc. 76 (11) (1993) 2707–2805.

[21] W. Widiyastuti, R. Balgis, F. Iskandar, K. Okuyama, Nanoparticle formation in spray pyrolysis under low temperature conditions, Chem. Eng. Sci. 65 (2010) 1846–1854.

[22] R.J. Lang, Ultrasonic atomization of liquids, J. Acoust. Soc. Am. 34 (1962) 6–8.

[23] B.E. Poling, J.M. Prausnitz, J.P. O'Connell, The properties of gases and liquids, 5th ed., Mc. Graw-Hill Inc., New York, 2011.

[24] T.T. Kodas, M. Hampden-Smith, Aerosol processing of materials, WILEY-VCH, 1999.

[25] W. Widiyastuti, W-N. Wang, I.W. Lenggoro, F. Iskandar, K. Okuyama, Simulation and experimental study of spray pyrolysis of polydispersed droplets, J. Mater. Res. 22 (7) (2007) 1868–1896.

[26] C. Zhang, L. Sun, Y. Zhang, C. Yan, Rare earth upconversion nanophosphors:synthesis, functionalization and application as biolabels and energy transfer donors, J. Rare Earths 28 (6) (2010) 807–819.

[27] F. Vetrone, J-C. Boyer, A. Capobianko, A. Speghini, M. Bettinelli, Significance of Yb^{3+} concentration on the upconversion mechanisms in codoped Y_2O_3: Er^{3+}, Yb^{3+} nanocrystals, J. Appl. Phys. 96 (1) (2004) 661–667.